ACS OMEGA

Open Access

http://pubs.acs.org/journal/acsodf

Article

Influence of Zirconium (Zr^{4+}) Substitution on the Crystal Structure and Optical and Dielectric Properties of $Sr_{0.8}Mg_{0.2}(Sn_{1-x}Zr_x)O_3$ Ceramics

Muhammad Anas, Asad Ali,* Abdul Ghaffar Khan, Aiyeshah Alhodaib,* Abid Zaman,* Tanveer Ahmad, Vineet Tirth, Ali Algahtani, Shohab Ahmad, Barno Sayfutdinovna Abdullaeva, Tawfiq Al-Mughanam, and Muhammad Aslam

Cite This: *ACS Omega* 2023, 8, 33794−33801

Read Online

ACCESS | Metrics & More | Article Recommendations

ABSTRACT: In this work, new compositions of $Sr_{0.8}Mg_{0.2}(Sn_{1-x}Zr_x)O_3$ $0.00 \leq x \leq 0.06$ ceramics are designed and synthesized by the conventional solid-state route. The influence of Zr doping on the phase, microstructural, optical, and dielectric properties is thoroughly investigated. The peaks (0 0 4) and (1 1 0) are observed to shift toward lower 2θ values, due to the variation of the ionic radius between Zr^{4+} and Sn^{4+}. X-ray diffraction patterns reveal the orthorhombic structure with the space group *Pbnm*. Scanning electron microscopy images reveal the presence of pores and particles with a high degree of agglomeration. The functional groups and modes of vibration are determined by Fourier transform infrared spectroscopy of the prepared metal oxide samples. The existence of green emission of all the synthesized samples around 554.91 nm is identified by photoluminescence spectroscopy. The dielectric properties of the fabricated samples are measured by using an impedance analyzer. The values of the tangent loss and relative permittivity are found to decrease with increasing frequency.

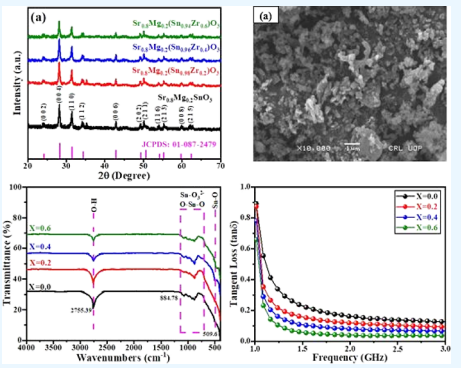

INTRODUCTION

Stannate perovskites, i.e., $MSnO_3$ (where M = Sr, Ca, or Ba) are ceramics with technical and industrial interests. Semiconductor sensors (for humidity and gases), energy storage, and barrier layer capacitors have been reported as applications of stannates.[1−5] Stannate synthesis routes are especially interesting because of their importance. Stannates have already been successfully synthesized using a variety of techniques, i.e., high-temperature solid-state reactions of $M(NO_3)_2/SnO_2$ or MCO_3/SnO_2 powder mixtures at different temperatures, i.e., 1000−1450 °C.[6−12] In addition to these ceramic preparation methods, those stannates can also be made by using sol−gel processes or by thermally decomposing oxalates.[13] However, the temperatures needed for these two alternate methods are 800 or 1000 °C, respectively. Low-temperature and quick synthesis methods are uncommon even with the numerous processes and characterizations of strontium stannate ($SrSnO_3$) that have been frequently investigated in the literature.[13−15] Long synthesis times are a feature of all of the ceramic routes for the stannates mentioned above (up to 16 h). As a result, it is clear that a more cost-effective, shorter-cycle, and lower-temperature synthesis process is required. The exciting process of microwave-assisted synthesis involves the synthesis of many inorganic compounds such as metals and oxides, as well as chloroformates, phosphates, etc., demonstrating the broad scope of applications for this technology.[16] Hydrothermal syntheses with microwave assistance method have also been carried out for several compositions.[17] Microwave dielectric ceramics with right relative permittivity (ε_r), high quality factor ($Q \times f$) values, and approximately zero temperature coefficient of resonant frequency have been extensively studied over the past few decades because they are essential components for microwave substrates, resonators, oscillators, and so on.[18−23] In addition, with the rapid development of wireless communication and the huge amount of information discovery since the start of the 21st century, there are new and higher requirements for microwave dielectric ceramics.[5,8,11] The focus of academic attention has shifted more and more toward investigating the upper limit of dielectric properties and looking for new low-loss candidates to meet emerging requirements. Based on this, we previously systematically investigated the synthesis of $Sr_3Ti_2O_7$ bulk ceramics and obtained excellent microwave dielectric proper-

Received: June 14, 2023
Accepted: August 31, 2023
Published: September 8, 2023

ties (ε_r = 63, $Q \times f$ = 84,000 GHz, and τ_f = 293 ppm/°C).[24] It has also been reported that compared to commercially available materials systems like $CaTiO_3$-$NdAlO_3$ (ε_r = 45, $Q \times f$ = 44,000 GHz, τ_f = +3 ppm/°C) and $CaLa_4Ti_4O_{15}$ (ε_r = 41.6, $Q \times f$ = 34,911 GHz, τ_f = −25 ppm/°C), the $Sr_3Ti_2O_7$ ceramics show optimum microwave dielectric properties without noble elements.[25−27] However, the large positive τ_f value needs to be further optimized because it is unsuitable for real-world use. Colla et al. concluded from a summary of structural parameters and microwave dielectric characteristics of complex perovskite ceramics based on Ba/Sr that the onset of octahedral tilting is the primary factor in determining the τ_f values.[28] The reason is that the doped Zr^{4+} ions have a higher ionic radius (0.72 Å) compared to Sn^{4+} (0.69 Å). The grain size of the samples increases gradually with increasing Zr doping concentrations, which indicates that Zr doping increases the number of defect sites to promote the formation of multiple nucleation centers.[29−31]

In the present study, an effort is made to synthesize $Sr_{0.8}Mg_{0.2}(Sn_{1-x}Zr_x)O_3$ lead-free ceramics ($0 \le x \le 0.6$) samples at frequencies 1.00−3.00 GHz via a conventional solid-state route. The solid-state route is a mechanical technique that is broadly used to grind powders into fine particles, and its effect on the crystallite size, dielectric properties, and microstructure development of milled powders is studied. Due to this importance, we studied the effect of Zr^{4+} on the relationship between the structural, microstructural, vibrational, and dielectric properties (dielectric constant and tangent loss) of $Sr_{0.8}Mg_{0.2}(Sn_{1-x}Zr_x)O_3$ materials which by varying the frequency are improved obviously.

RESULTS AND DISCUSSION

Phase Analysis. The X-ray diffraction (XRD) pattern of sintered $Sr_{0.8}Mg_{0.2}(Sn_{1-x}Zr_x)O_3$ ($0.0 \le x \le 0.6$) ceramics is shown in Figure 1. An X-ray powder diffractometer (JDX-3532, JEOL, Japan) using Cu Kα radiation (λ = 0.154 nm) within the angular range of Bragg's angle, i.e., 2θ = 20−80°, was used for phase identification and structural characterization of materials.

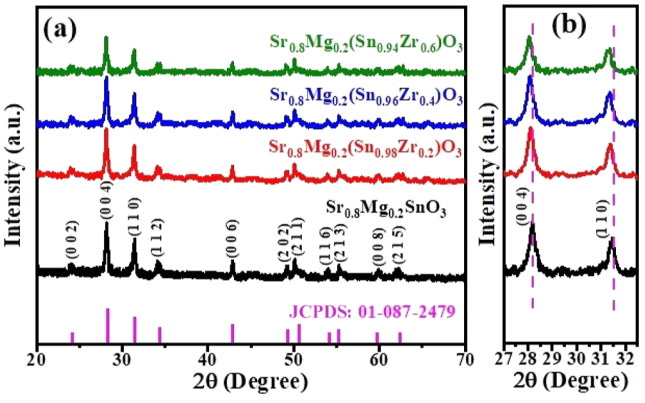

Figure 1. (a) $Sr_{0.8}Mg_{0.2}(Sn_{1-x}Zr_x)O_3$ ($0.0 \le x \le 0.6$) ceramic XRD pattern and (b) zoomed-in view of (0 0 4) and (1 1 0) peaks shifting toward the lower angle.

The XRD patterns of all the diffracted peaks indicate the smooth crystalline structure of the samples. XRD analysis confirmed the presence of an orthorhombic structure with lattice parameters (a = 3.80 Å, b = 6.33 Å, and c = 14.60 Å) and having the space group of ($Pbnm$) that are consistent with the JCPDS/ICDD card info [01-087-2479] for the base sample. The most intense peaks (004) and (110) observed at angular positions 28.2 and 31.5°, respectively, are found to be shifted toward a lower angle (2θ = 31.2°) for all samples, as shown in Figure 1b. The shifting of peaks may be associated with the increase of the volume of the unit cell due to replacing SnO_3 with $(Sn_{1-x}Zr_x)O_3$, wherein Zr^{4+} has a high ionic radius (0.72 Å) compared to Sn^{4+} (0.69 Å).[32,33]

According to Bragg's law, the angular position (θ) is inverse to the lattice spacing (d), i.e., $\theta \propto 1/d$.[34,35] The size of crystal (D) of a sample should be measured by using the Scherrer formula[36]

$$D = \frac{\kappa\lambda}{\beta\cos\theta} = \frac{0.9\lambda}{\beta\cos\theta} \quad (1)$$

where λ is the wavelength of Cu Kα radiation, θ is the angular position of the diffraction peak, and β is the fwhm, while the crystalline size depends on the microstrain of the lattice and the radius of the substituted ions. The enlargement in the calculated crystallite size is due to the distortion in the host Sn^{4+} lattice by the foreign impurities of Zr^{4+}.

Mathematically, the micro-strain (s) and the dislocation density (δ) will be measured by using the following equations[36]

$$\delta = \frac{1}{D^2} \quad (2)$$

$$s = \frac{d}{D\sqrt{12}} \quad (3)$$

The dislocation of the material had a significant impact on the structure and dielectrics of the material. Due to the dopant element, the crystal structure of the material was improved, and crystal defects were significantly reduced due to the proper replacement of host ions within the lattice of the crystal. Using the below equation,[37] we were able to determine the lattice strain (η).

$$\eta = \frac{\beta\cos\theta}{4} \quad (4)$$

The deviancy in measured values of lattice strain and crystallite size of all the synthesized $Sr_{0.8}Mg_{0.2}(Sn_{1-x}Zr_x)O_3$ ($0.0 \le x \le 0.6$) ceramic samples with composition are shown in Table 1. The microstrain decreases with increasing dopant concentration, which might be due to the size of the dopant element being greater than that of the host element (see Table 1).

Morphological Analysis. The morphological properties of all samples were recorded at the same magnification of ×10,000 (1 μm) and is shown in Figure 2a−d. It depicts the microstructure that expressively shows the dissemination of

Table 1. Crystallite Size (D), Dislocation Density (δ), Lattice Strain (η), and Microstrain (ε) Were All Determined for $Sr_{0.8}Mg_{0.2}(Sn_{1-x}Zr_x)O_3$ ($0.0 \le x \le 0.6$) Ceramics

parameters	X = 0.0	X = 0.2	X = 0.4	X = 0.6
average crystallite size "D" (nm)	3.5735	5.1358	8.0364	7.5885
dislocation density "δ" ($\times 10^{-2}$) nm^{-2}	7.8310	3.7912	1.5584	1.7437
lattice strain "η" ($\times 10^{-3}$)	0.0970	0.0675	0.0431	0.0457
microStrain "ε" ($\times 10^{-2}$)	1.4291	0.9941	0.6359	0.6747

https://doi.org/10.1021/acsomega.3c04224
ACS Omega 2023, 8, 33794−33801

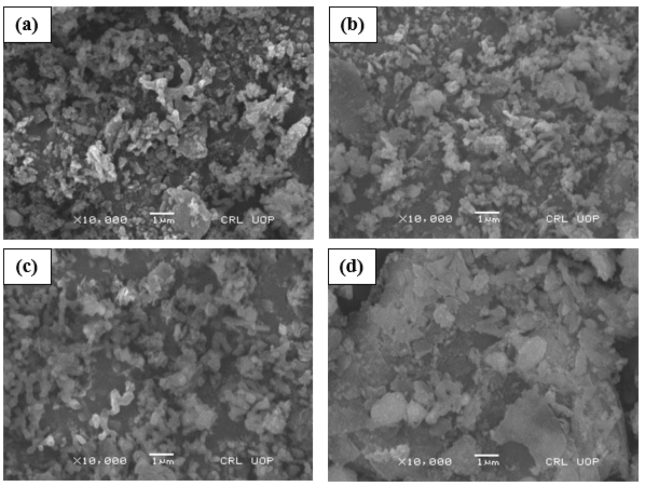

Figure 2. SEM images of (a) $Sr_{0.8}Mg_{0.2}SnO_3$, (b) $Sr_{0.8}Mg_{0.2}(Sn_{0.98}Zr_{0.2})O_3$, (c) $Sr_{0.8}Mg_{0.2}(Sn_{0.96}Zr_{0.4})O_3$, and (d) $Sr_{0.8}Mg_{0.2}(Sn_{0.94}Zr_{0.6})O_3$.

grain size. The scanning electron microscopy (SEM) images revealed the grain size along with porosity. The grain size increased, while the porosity decreased with increasing Zr^{4+} content. Studies have demonstrated that the size and morphology of crystallites within compounds are affected by nucleation and the formation of grains during synthesis. Furthermore, particle morphology was also affected by the calcination temperature.[38,39]

Fourier Transform Infrared Spectroscopy. Figure 3 displays the Fourier transform infrared (FTIR) spectra of

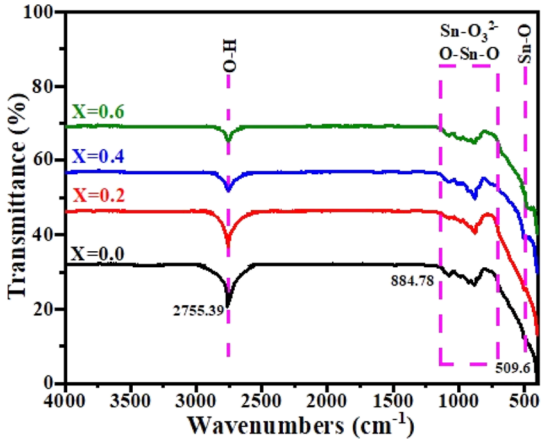

Figure 3. FTIR spectra of sintered ceramics with the formula $Sr_{0.8}Mg_{0.2}(Sn_{1-x}Zr_x)O_3$ $(0.0 \le x \le 0.6)$.

sintered $Sr_{0.8}Mg_{0.2}(Sn_{1-x}Zr_x)O_3$ $(0.0 \le x \le 0.6)$ ceramics. The FTIR spectra band positions and the absorption peaks are directly influenced by the material compositions, lattice microstrain, and shape of materials.[40] Normally, the IR spectrum under 1100 cm^{-1} is recognized as the deformations mode of the Sn−O octahedral (SnO_6) or O−Sn−O deformation bridge.[41] The bands at 400 and 900 cm^{-1} are related to the molecular vibration of Sn−O.[42] The absorption peak with high intensity at 884.78 cm^{-1} is due to the existence of vibration mode of $Sn-O_3^{2-}$. The highest absorption peak at 509.6 cm^{-1} was likewise connected to the stretching vibration of Sn−O bands, and this relationship verifies the occurrence of SnO_6 octahedral deformation in all compositions.[43] The material may experience O−H stretching vibrations as a result of absorbing ambient moisture, as seen by the steep peaks at 858 and 2755.39 cm^{-1}. The Sn−OH bonds' asymmetric stretching vibration is represented by the absorption peak. As a result, the FTIR investigation supports the materials' presence of active IR modes and metal oxide vibrations (see Figure 3).

Optical Studies. Figure 4 displays the UV−vis absorption spectra of sintered $Sr_{0.8}Mg_{0.2}(Sn_{1-x}Zr_x)O_3$ $(0.0 \le x \le 0.6)$. O−

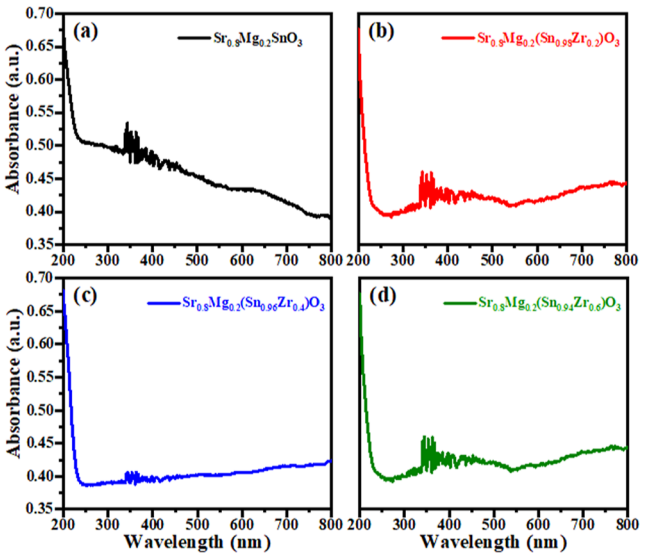

Figure 4. Absorption spectra of (a) $Sr_{0.8}Mg_{0.2}SnO_3$, (b) $Sr_{0.8}Mg_{0.2}(Sn_{0.98}Zr_{0.2})O_3$, (c) $Sr_{0.8}Mg_{0.2}(Sn_{0.96}Zr_{0.4})O_3$, and (d) $Sr_{0.8}Mg_{0.2}(Sn_{0.94}Zr_{0.6})O_3$.

M charge carrier transitions of the octahedral groups in SnO_6 may be responsible for the formation of a large maximum absorption peak in the 300−450 nm wavelength range.[44] The crystal size, microstrain, and shape of particles influence optical absorption, hence the difference between the spectra of pure and Zr-doped $Sr_{0.8}Mg_{0.2}SnO_3$ compounds. The lattice strain is particularly responsible for charge location at the interface and surface or interfacial trapping.[45] Increasing the dopant concentration caused a noticeable change in absorption, which led to the discovery of the likely electronic transitions between the host and dopant lattices. Previous research indicated that the spectral lines are influenced by the lattice's level of structural order or disorder.[46] Additionally, optical energy band gap (E_g) parameters correlate with the synthesis method, particle surface shape, precursor solution temperature, and pH. It should be mentioned that the degree of order or disorder is linked to the presence of impurities, oxygen vacancies, and distorted localization and caused the induction of extra electronic levels in stannates' prohibited band.[41] As a result, the $SrSnO_3$ compound's optical absorption was solely dependent on the shift from 2p oxygen localities to the 3d configuration of stannates. The Wood and Tauc equation was used to determine the optical energy band gap (E_g) of pristine and Zr-doped $Sr_{0.8}Mg_{0.2}SnO_3$ compounds, as shown in Figure 5.

$$\alpha h\upsilon = (h\upsilon - E_g)^n \tag{5}$$

where α is the absorbance factor, h is Planck's constant, υ is the frequency, and E_g is the band gap energy.[34]

https://doi.org/10.1021/acsomega.3c04224
ACS Omega 2023, 8, 33794−33801

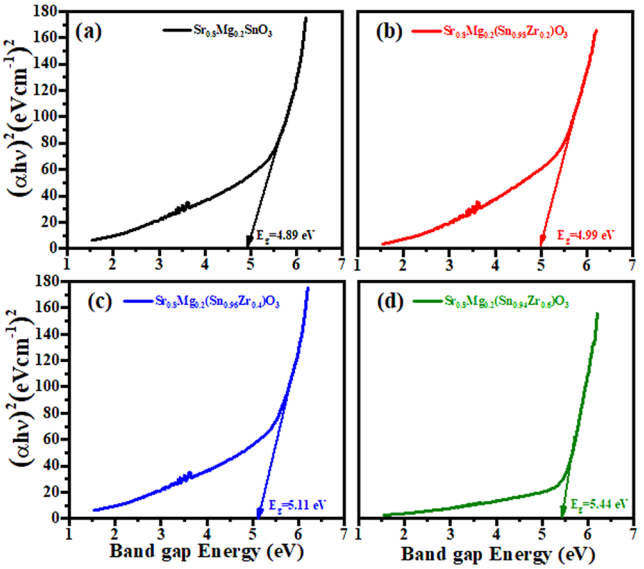

Figure 5. Band gap energies of (a) $Sr_{0.8}Mg_{0.2}SnO_3$, (b) $Sr_{0.8}Mg_{0.2}(Sn_{0.98}Zr_{0.2})O_3$, (c) $Sr_{0.8}Mg_{0.2}(Sn_{0.96}Zr_{0.4})O_3$, and (d) $Sr_{0.8}Mg_{0.2}(Sn_{0.94}Zr_{0.6})O_3$.

Perovskite-based compounds show direct permissible electronic transitions according to previous studies. The high optical absorbance observed in the present work suggests that all compounds exhibit direct permissible electronic transitions.[37] Figure 5 depicts the plot of E_g and $(\alpha h\nu)2$. The spectral band gap of the $Sr_{0.8}Mg_{0.2}SnO_3$ compound was determined from the plot to be 4.89 eV. The samples show the interdependent nature of absorption edge values and demonstrated the effects of lattice strain, crystalline structure, and variance on surface properties of the produced compounds.[47] Additionally, the band gap energy grows with Zr^{4+} concentration (see Figure 5). As a result, it can be inferred that the E_g is associated with the emergence of intermediate energy levels as a result of distortions on $[SnO_6]$ octahedrons, which supports the impact of Zr^{4+} incorporation into the $Sr_{0.8}Mg_{0.2}SnO_3$ system.

Photoluminescence Spectroscopy. Figure 6 shows the photoluminescence (PL) behavior of pure and Zr-doped $Sr_{0.8}Mg_{0.2}SnO_3$ sintered ceramics at room temperature. The PL features of the perovskite-like structure arise due to distortions of constellations located in this system. It is acknowledged that the PL emissions are significant for the order/disorder ratio in a sample.[48] In semiconductors, the PL characteristics depend upon the surface morphology and calcination temperature of the raw materials.[49,50] As a consequence, the production of medium-energy levels and the enabling of various energetic transitions between them led to the formation of the wide emission spectra that were seen in the samples.[22]

The PL spectra observed in the region of 800−400 nm at the exciting wavelength λ_{ex} = 550 nm and energy = 2.24 eV are given in Figure 6 in order to study optical properties of the synthesized $Sr_{0.8}Mg_{0.2}(Sn_{1-x}Zr_x)O_3$ $(0.0 \leq x \leq 0.6)$ solid solution. The energy of each peaks are calculated by eq 6.[51,52]

$$E = \frac{hc}{\lambda} \tag{6}$$

The PL spectra (Figure 6) have been deconvoluted for each sample properly.[53,54] We have calculated the value of excitation potential energy of each peaks observed at wavelengths 422, 466.75, 554.27, 671.12, 690.76, 705.44, and 757 nm as 2.95, 2.66, 2.24, 1.85, 1.80, 1.76, and 1.64 eV, respectively. The slight energy difference occurring with increasing Zr^{4+} concentration was due to the presence of oxygen vacancies, formation of defects, and quantum confinements.[52] Generally speaking, it was said that the synthesis process, which affects the form, size, and crystalline nature of the particles, was closely related to the luminous efficiency.[55] In addition, it was found that the luminosity of $SrSnO_3$ compounds is mainly affected by the particle size.[52] In Figure 6, green emission of the entire synthesized samples is observed around 554.91 nm,

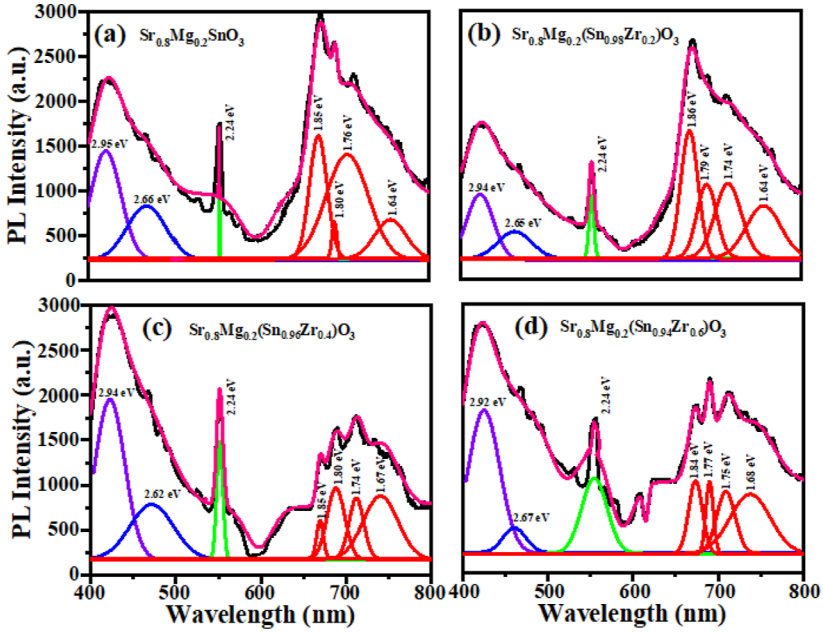

Figure 6. PL spectrum of ceramics: (a) $Sr_{0.8}Mg_{0.2}SnO_3$, (b) $Sr_{0.8}Mg_{0.2}(Sn_{0.98}Zr_{0.2})O_3$, (c) $Sr_{0.8}Mg_{0.2}(Sn_{0.96}Zr_{0.4})O_3$, and (d) $Sr_{0.8}Mg_{0.2}(Sn_{0.94}Zr_{0.6})O_3$.

https://doi.org/10.1021/acsomega.3c04224
ACS Omega 2023, 8, 33794−33801

and the identified peak corresponds to direct transitions between O 2p and Sn 5s energy states.[56,57]

Microwave Dielectric Properties. Figures 7 and 8 illustrate the frequency dependence of the microwave dielectric

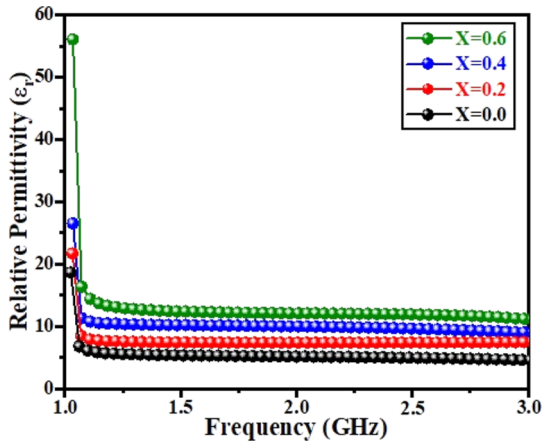

Figure 7. $Sr_{0.8}Mg_{0.2}(Sn_{1-x}Zr_x)O_3$ $(0.0 \le x \le 0.6)$ sintered ceramics exhibit frequency-dependent changes in relative permittivity.

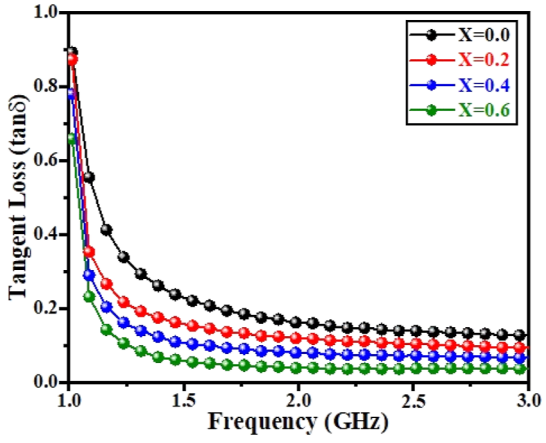

Figure 8. Variation of tangent loss with the frequency of $Sr_{0.8}Mg_{0.2}(Sn_{1-x}Zr_x)O_3$ $(0.0 \le x \le 0.6)$ ceramics.

characteristics (i.e., dielectric constant and tangent loss) of the sintered ceramic samples of $Sr_{0.8}Mg_{0.2}(Sn_{1-x}Zr_x)O_3$ $(0.0 \le x \le 0.6)$. The graph character indicates the dispersion of the material as well as the effects of blocking. The main reasons for this dispersion are the related mobile charge carriers as well as the polarized composition of the sample studied.[58] The presence of several polarizations such as dipolar and ionic electronic polarizations as well as interfacial polarizations may be influenced by the large dielectric constant dispersions.[9,25,59,60] By application of the local field, the electrons inside the material move opposite to the field by a small displacement (dipole moment) resulting in electronic polarization, and this behavior occurs above 1 GHz operating frequency.[61] Moreover, the dielectric constant decreases with frequency (see Figure 7); it is due to the permanent dipole moments which further affected the overall polarization mechanism inside the material. At a high frequency, the field changes for strong dipole moments which orient in the direction of the field. This dipole moment is never sustained for a long time inside the material, and it is the main cause of variation of dielectric constant with frequency.[62] So, the value of the dielectric constant decreases with frequency, as has been reported in our work. Figure 8 shows the variation of dielectric loss or tangent loss (tan δ) with frequency as well. This variation in tangent loss is due to the relaxation mechanism. The increase in tangent loss shows the existence of a hopping mechanism (frequency-dependent) in the sample, which was due to the charge carrier phenomenon.[63] Dielectric materials may increase the storage capacity of electronic devices. So, the capacitance of a material is directly associated with the dielectric constant.[64,65] The dielectric constant can be measured as

$$\varepsilon_r = \frac{\varepsilon_m}{\varepsilon_0} \tag{7}$$

where "ε_r" is the dielectric constant, "ε_m" is the permittivity of medium, while "ε_0" is the permittivity of free space. The permittivity of medium can be determined by using the following equation

$$\varepsilon_m = \frac{Cd}{\varepsilon_0 A} \tag{8}$$

Here, "C" is the capacitance of material calculated by the impedance analyzer "d" is the thickness of pellets, and "A" is the area of pellets.

In a perfect dielectric, if an ac voltage is applied across a capacitor, then the charging current leads the applied voltage by phase angle 90. But in commercial use, due to some defects or leakage current, the phase angle 90 is disturbed by the amount of "δ", called the loss angle, and causes the power dissipation in the material. So, the tangent loss can be calculated as

$$\tan\delta = \frac{1}{2\pi f C_p R_p} \tag{9}$$

Here, "C_p" and "R_p" are, respectively, the measured parallel capacitance and resistance at frequency "f". A commonly used technique for device miniaturization involves the placement of materials with high dielectric constants at the local level of the structure, taking into account the distribution of electromagnetic fields at the operating frequencies of the device.[66]

CONCLUSIONS

In this work, pure and Zr-doped $Sr_{0.8}Mg_{0.2}SnO_3$ compounds synthesized by the mixed oxide route have been investigated. The XRD patterns reveal the materialization of the orthorhombic phase with the space group (*Pbnm*). The metal oxide vibrations of all the samples were analyzed via FTIR spectra. The SEM images revealed that the particle size increases with the Zr^{4+} content and there is a high degree of agglomeration. The absorption spectrum confirmed the good optical behaviors of all the samples. The emission center does not change by the addition of Zr^{4+} in $Sr_{0.8}Mg_{0.2}SnO_3$ sintered ceramics, as investigated by PL analysis. Optical band gap energy is increased with the content of Zr^{4+}. The dissipation factor decreases with increasing frequency and Zr^{4+} contents. The reducing dissipation factor for this material renders it suitable for the application of device miniaturization.

EXPERIMENTAL METHODS

Synthesis of $Sr_{0.8}Mg_{0.2}(Sn_{1-x}Zr_x)O_3$ (x = 0, 0.2, 0.4, 0.6) ceramics was done through a mixed oxides route using materials of high purity such as $SrCO_3$ (Merck) (99.99%),

https://doi.org/10.1021/acsomega.3c04224
ACS Omega 2023, 8, 33794−33801

SnO_2 (Merck) (99.99%), $MgCO_3$ (Aladdin Biochemical Technology Co., Ltd., Shanghai, China), and ZrO_2 (Merck) (99.99%). Stoichiometric concentrations of oxides were weighed and ball-milled (wetting media) for 24 h. The solution was dried at 80 °C in an oven. After drying, the powder mixture was calcined at 900 °C for 3 h to achieve high purity in alumina crucibles. To avoid agglomeration, the calcined powder was manually ground by using mortar and pestle for 1 h. The powder was made into 10 mm diameter pallets, and the thickness of pellets was 5 mm under 5 ton/in^2 pressure using a pellet pressor (Carver, USA). After pellet' formation, the pellets were sintered at a temperature of 800 °C for 3 h with a heating and cooling rate of 5 °C/min. The phase formation was analyzed by using an X-ray diffractometer (JDX-3532, JEOL, Japan) with Cu Kα (λ = 0.15406 nm). The sample density was measured by using an electronic densitometer (MD-3005). The surface morphological study of the samples was carried out by a scanning electron microscope (JEOL 7600F) operated at 15 KV. The absorption spectrum of the samples was recorded by using the FTIR spectrometer (PerkinElmer GX) to obtain 10 cm^{-1} spectral resolution in the range of 400−4000 cm^{-1} region. The UNICO 2150-UV spectrophotometer was used to measure the sample's absorbance of light in the UV−vis range. To measure the PL spectrum, a Jobin Yvon-Horiba Triax 190 was used with a spectral resolution of 0.30 nm. For the purpose of determining the dielectric characteristics of the sintered ceramic samples, an instrument known as a VNA (vector network analyzer) (ZVB20, Schwarz & Rohde, Germany) was utilized.

AUTHOR INFORMATION

Corresponding Authors

Asad Ali − *Department of Physics, Government Postgraduate College Nowshera, Nowshera, Khyber Pakhtunkhwa 24100, Pakistan*; Email: kasadiiui@gmail.com

Aiyeshah Alhodaib − *Department of Physics, College of Science, Qassim University, Buraydah 51452, Saudi Arabia*; Email: ahdieb@qu.edu.sa

Abid Zaman − *Department of Physics, Riphah International University, Islamabad 44000, Pakistan*; orcid.org/0000-0001-9527-479X; Email: zaman.abid87@gmail.com

Authors

Muhammad Anas − *Department of Physics, Abdul Wali Khan University Mardan, Mardan 23200, Pakistan*

Abdul Ghaffar Khan − *Department of Physics, Government Postgraduate College Nowshera, Nowshera, Khyber Pakhtunkhwa 24100, Pakistan*

Tanveer Ahmad − *Department of Physics, Abdul Wali Khan University Mardan, Mardan 23200, Pakistan*; orcid.org/0000-0002-7021-7024

Vineet Tirth − *Mechanical Engineering Department, College of Engineering, King Khalid University, Abha, Asir 61421, Kingdom of Saudi Arabia; Research Center for Advanced Materials Science (RCAMS), King Khalid University, Abha, Asir 61413, Kingdom of Saudi Arabia*; orcid.org/0000-0002-8208-7183

Ali Algahtani − *Mechanical Engineering Department, College of Engineering, King Khalid University, Abha, Asir 61421, Kingdom of Saudi Arabia; Research Center for Advanced Materials Science (RCAMS), King Khalid University, Abha, Asir 61413, Kingdom of Saudi Arabia*

Shohab Ahmad − *Department of Electrical and Computer Engineering, COMSATS University Islamabad, Abbottabad 22044, Pakistan*

Barno Sayfutdinovna Abdullaeva − *Professor, Doctor of Pedagogical Sciences, Vice-Rector for Scientific Affairs, Tashkent State Pedagogical University, Tashkent 100027, Uzbekistan*

Tawfiq Al-Mughanam − *Department of Mechanical Engineering, College of Engineering, King Faisal University, Al-Ahsa 31982, Saudi Arabia*

Muhammad Aslam − *Institute of Physics and Technology, Ural Federal University, Yekaterinburg 620002, Russia*

Complete contact information is available at: https://pubs.acs.org/10.1021/acsomega.3c04224

Notes

The authors declare no competing financial interest.

ACKNOWLEDGMENTS

The authors extend their appreciation to the Deanship of Scientific Research at King Khalid University Abha 61421, Asir, Kingdom of Saudi Arabia, for funding this work through the Large Groups Project under grant number RGP.2/498/44. The authors acknowledge the Deanship of Scientific Research, Vice Presidency for Graduate Studies and Scientific Research at King Faisal University, Saudi Arabia, for financial support under the annual funding track [GRANT4110].

REFERENCES

(1) Doroftei, C.; Popa, P. D.; Iacomi, F. Study of the influence of nickel ions substitutes in barium stannates used as humidity resistive sensors. *Sens. Actuators, A* **2012**, *173*, 24−29.

(2) Kumar, A.; Khan, B.; Yadav, V.; Dixit, A.; Kumar, U.; Singh, M. K. Rietveld refinement, optical, dielectric and ac conductivity studies of Ba-doped SrSnO3. *J. Mater. Sci.: Mater. Electron.* **2020**, *31*, 16838−16848.

(3) Yoon, D.; Yu, S.; Son, J. Oxygen vacancy-assisted recovery process for increasing electron mobility in n-type BaSnO3 epitaxial thin films. *NPG Asia Mater.* **2018**, *10*, 363−371.

(4) Kumar, A.; Choudhary, R. N. P.; Singh, B. P.; Thakur, A. K. Effect of strontium concentration on electrical conduction properties of Sr-modified BaSnO3. *Ceram. Int.* **2006**, *32*, 73−83.

(5) Murauskas, T.; Kubilius, V.; Saltyte, Z.; Plausinaitiene, V. Metalorganic chemical vapor deposition and investigation of non-stoichiometry of undoped BaSnO3 and La-doped BaSnO3 thin films. *Thin Solid Films* **2019**, *692*, 137575.

(6) Chen, D.; Ye, J. SrSnO3 nanostructures: synthesis, characterization, and photocatalytic properties. *Chem. Mater.* **2007**, *38*, 4585−4591.

(7) Stanulis, A.; Selskis, A.; Ramanauskas, R.; Beganskiene, A.; Kareiva, A. Low temperature synthesis and characterization of strontium stannate−titanate ceramics. *Mater. Chem. Phys.* **2011**, *130*, 1246−1250.

(8) Dohnalová, Ž.; Šulcová, P.; Bělina, P. Pink NIR pigment based on Cr-doped $SrSnO_3$, Preparation and characterization. *J. Therm. Anal. Calorim.* **2019**, *138*, 4475−4484.

(9) Mishra, G.; Minor, C.; Tiwari, A. High throughput synthesis of BaSnO3 microcrystals by molten salt technique. *Mater. Chem. Phys.* **2023**, *295*, 127042.

(10) Mizoguchi, H.; Woodward, P. M.; Park, C. H.; Keszler, D. A. Strong near-infrared luminescence in BaSnO3. *J. Am. Chem. Soc.* **2004**, *35*, 9796−9800.

(11) Khirade, P. P. Structural, microstructural and magnetic properties of sol−gel-synthesized novel BaZrO 3−CoFe 2 O 4 nanocomposite. *J. Nanostruct. Chem.* **2019**, *9*, 163−173.

https://doi.org/10.1021/acsomega.3c04224
ACS Omega 2023, 8, 33794−33801

(12) Sharma, N.; Shaju, K. M.; Rao, G. S.; Chowdari, B. V. R. Anodic behaviour and X-ray photoelectron spectroscopy of ternary tin oxides. *J. Power Sources* **2005**, *139*, 250−260.
(13) Kurre, R.; Bajpai, S.; Bajpai, P. K. Synthesis, Characterization, Optical and Transport Properties of BaSnO₃ Synthesized by Wet Chemical Route. *Mater. Sci. Appl.* **2018**, *09*, 92−110.
(14) Cernea, M.; Trusca, R.; Radu, R.; Valsangiacom, C. Ba (Ti1−xSnx) O3 (x= 0.13) nanomaterials produced by low-temperature aqueous synthesis. *J. Alloys Compd.* **2011**, *509*, 9934−9937.
(15) Udawatte, C. P.; Kakihana, M.; Yoshimura, M. Low temperature synthesis of pure SrSnO3 and the (BaxSr1−x)SnO3 solid solution by the polymerized complex methodx) SnO3 solid solution by the polymerized complex method. *Solid State Ionics* **2000**, *128*, 217−226.
(16) Bilecka, I.; Djerdj, I.; Niederberger, M. One-minute synthesis of crystalline binary and ternary metal oxide nanoparticles. *Chem. Commun.* **2008**, 886−888.
(17) Komarneni, S.; Roy, R.; Li, Q. H. Microwave-hydrothermal synthesis of ceramic powders. *Mater. Res. Bull.* **1992**, *27*, 1393−1405.
(18) Vanderah, T. A. Talking ceramics. *Science* **2002**, *298*, 1182−1184.
(19) Reaney, I. M.; Iddles, D. Microwave dielectric ceramics for resonators and filters in mobile phone networks. *J. Am. Ceram. Soc.* **2006**, *89*, 2063−2072.
(20) Sebastian, M. T.; Ubic, R.; Jantunen, H. Low-loss dielectric ceramic materials and their properties. *Int. Mater. Rev.* **2015**, *60*, 392−412.
(21) Huang, Y. H.; Liu, B.; Song, K. X. Microwave dielectric properties of temperature stable (1-x) SrLaAlO4-xTiO2 composite ceramics. *Ceram. Int.* **2018**, *44*, S125−S128.
(22) Liu, B.; Liu, X. Q.; Chen, X. M. Sr2LaAlTiO7: a new Ruddlesden−Popper compound with excellent microwave dielectric properties. *J. Mater. Chem. C* **2016**, *4*, 1720−1726.
(23) Lee, C. H.; Orloff, N. D.; Birol, T.; Zhu, Y.; Goian, V.; Rocas, E.; Haislmaier, R.; Vlahos, E.; Mundy, J. A.; Kourkoutis, L. F.; Nie, Y.; et al. Exploiting dimensionality and defect mitigation to create tunable microwave dielectrics. *Nature* **2013**, *502*, 532−536.
(24) Liu, B.; Li, L.; Liu, X. Q.; Chen, X. M. $Sr_{<i>n</i>+1}Ti_{<i>n</i>}O_{3<i>n</i>+1}$(n=1, 2) microwave dielectric ceramics with medium dielectric constant and ultra-low dielectric loss. *J. Am. Ceram. Soc.* **2017**, *100*, 496−500.
(25) Harkiah, S.; Rauf, N.; Tahir, D. Review of ceramic materials and recent development of preparation methods. *Gravitasi* **2022**, *21*, 49−60.
(26) Zang, X.; Ma, W.; Niu, B.; Li, N.; Wang, Y. The microwave dielectric properties of CaxBi4−xTi3O12−x/2 (0.0 ≤ x ≤ 1.4) ceramics. *J. Mater. Sci.: Mater. Electron.* **2016**, *27*, 8105−8110.
(27) Wise, P. L.; Reaney, I. M.; Lee, W. E.; Price, T. J.; Iddles, D. M.; Cannell, D. S. Structure−microwave property relations in (SrxCa(1−x))n+1TinO3n+1x)) n+ 1TinO3n+ 1. *J. Eur. Ceram. Soc.* **2001**, *21*, 1723−1726.
(28) Park, H. S.; Yoon, K. H.; Kim, E. S. Effect of bond valence on microwave dielectric properties of complex perovskite ceramics. *Mater. Chem. Phys.* **2003**, *79*, 181−183.
(29) Hu, Y.; Shi, Q.; Huang, W.; Zhu, H.; Yue, F.; Xiao, Y.; Liang, S.; Lu, T.; Lu, T. Preparation and phase transition properties of Ti-doped VO 2 films by sol−gel process. *J. Sol-Gel Sci. Technol.* **2016**, *78*, 19−25.
(30) Khirade, P. P.; Raut, A. V.; Alange, R. C.; Barde, W. S.; Chavan, A. R. Structural, electrical and dielectric investigations of cerium doped barium zirconate (BaZrO3) nano-ceramics produced via green synthesis: Probable candidate for solid oxide fuel cells and microwave applications. *Phys. B* **2021**, *613*, 412948.
(31) Khirade, P. P.; Birajdar, S. D.; Humbe, A. V.; Jadhav, K. M. Structural, electrical and dielectrical property investigations of Fe-doped BaZrO 3 nanoceramics. *J. Electron. Mater.* **2016**, *45*, 3227−3235.
(32) *Microwave Materials and Applications, 2 Volume Set*; Sebastian, M. T., Ubic, R., Jantunen, H., Eds.; John Wiley & Sons, 2017.
(33) Kumar, U.; Yadav, D.; Upadhyay, S. Investigation of structural, optical, and magnetic properties of Nd-doped Sr2SnO4 Ruddlesden Popper oxide. *J. Am. Ceram. Soc.* **2020**, *103*, 5743−5757.
(34) Vinayak, V.; Khirade, P. P.; Birajdar, S. D.; Alange, R. C.; Jadhav, K. M. Electrical and dielectrical properties of low-temperature-synthesized nanocrystalline Mg 2+-substituted cobalt spinel ferrite. *J. Supercond. Novel Magn.* **2015**, *28*, 3351−3356.
(35) Kumar, U.; Upadhyay, S. Structural, optical, and electrical properties of Ruddlesden Popper oxide Ba2SnO4. *J. Electron. Mater.* **2019**, *48*, 5279−5293.
(36) Zaman, A.; Uddin, S.; Mehboob, N.; Ali, A. Structural investigation and improvement of microwave dielectric properties in Ca (HfxTi1-x) O3 ceramics. *Phys. Scr.* **2020**, *96*, 025701.
(37) Zaman, A.; Uddin, S.; Mehboob, N.; Ali, A.; Ahmad, A.; Bashir, K. Effect of Zr4+ on the structural and microwave dielectric properties of CaTiO3 ceramics. *Ferroelectrics* **2021**, *577*, 143−152.
(38) Wang, S.; Lu, M.; Zhou, G.; Zhang, H.; Yang, Z. Systematic investigations into SrSnO3 nanocrystals (II) photoluminescent properties of the as-synthesized nanocrystals. *J. Alloys Compd.* **2008**, *452*, 432−434.
(39) Melo, D.; Marinho, R. M. M.; Vieira, F. T. G.; Lima, S. J. G.; Longo, E.; Souza, A. G.; Maia, A. S.; Santos, I. M. G. Influence of Cu (II) in the SrSnO 3 crystallization. *J. Therm. Anal. Calorim.* **2011**, *106*, 513−517.
(40) Ouni, S.; Nouri, S.; Rohlicek, J.; Ben Hassen, R. Structural and electrical properties of the sol−gel prepared Sr1− xErxSnO3− δ compounds. *J. Solid State Chem.* **2012**, *192*, 132−138.
(41) Bohnemann, J.; Libanori, R.; Moreira, M. L.; Longo, E. High-efficient microwave synthesis and characterisation of SrSnO3. *Chem. Eng. J.* **2009**, *155*, 905−909.
(42) Alves, M. C.; Nascimento, M. R.; Lima, S. J.; Pizani, P. S.; Espinosa, J. W.; Longo, E.; Soledade, L. E.; Souza, A. G.; Santos, I. M.; Santos, I. M. Influence of synthesis conditions on carbonate entrapment in perovskite SrSnO3. *Mater. Lett.* **2009**, *63*, 118−120.
(43) Zaman, A.; Uddin, S.; Mehboob, N.; Tirth, V.; Algahtani, A.; Abbas, M.; Mushtaq, M.; Ali, A.; Sultana, F.; Althubeiti, K.; et al. Structural Elucidation, Electronic and Microwave Dielectric Properties of $Ca(Sn_{<i>x</i>}Ti_{1-<i>x</i>})O_3$, (0 ≤ x ≤ 0.8) Lead-Free Ceramics. *ACS Omega* **2022**, *7*, 4667−4676.
(44) Stanulis, A.; Sakirzanovas, S.; Van Bael, M.; Kareiva, A. Sol−gel (combustion) synthesis and characterization of different alkaline earth metal (Ca, Sr, Ba) stannates. *J. Sol-Gel Sci. Technol.* **2012**, *64*, 643−652.
(45) Lee, C. W.; Kim, D. W.; Cho, I. S.; Park, S.; Shin, S. S.; Seo, S. W.; Hong, K. S. Simple synthesis and characterization of SrSnO3 nanoparticles with enhanced photocatalytic activity. *Int. J. Hydrogen Energy* **2012**, *37*, 10557−10563.
(46) Ashokkumar, M.; Muthukumaran, S. Tuning of energy gap, microstructure, optical and structural properties of Cr doped Zn0. 96Cu0.04O nanoparticles. *Powder Technol.* **2014**, *258*, 157−164.
(47) Alves, M. C.; Nascimento, M. R.; Lima, S. J.; Pizani, P. S.; Espinosa, J. W.; Longo, E.; Soledade, L. E.; Souza, A. G.; Santos, I. M. Influence of synthesis conditions on carbonate entrapment in perovskite SrSnO3. *Mater. Lett.* **2009**, *63*, 118−120.
(48) Wang, S.; Lu, M.; Zhou, G.; Zhang, H.; Yang, Z. Systematic investigations into SrSnO3 nanocrystals (II) photoluminescent properties of the as-synthesized nanocrystals. *J. Alloys Compd.* **2008**, *452*, 432−434.
(49) Patel, D. K.; Sengupta, A.; Vishwanadh, B.; Sudarsan, V.; Vatsa, R. K.; Kadam, R.; Kumar Kulshreshtha, S. Local Environments Around Eu3+ and Eu2+ Ions in Dual Light-Emitting BaSnO3: Eu Nanomaterials. *Eur. J. Inorg. Chem.* **2012**, *2012*, 1609−1619.
(50) Dohnalová, Ž.; Gorodylova, N.; Šulcová, P.; Vlček, M. Synthesis and characterization of terbium-doped SrSnO3 pigments. *Ceram. Int.* **2014**, *40*, 12637−12645.

https://doi.org/10.1021/acsomega.3c04224
ACS Omega 2023, 8, 33794−33801

(51) Ali, A.; Uddin, S.; Lal, M.; Zaman, A.; Iqbal, Z.; Althubeiti, K. Structural, optical and microwave dielectric properties of Ba (Ti1− xSnx) 4O9, 0≤ x≤ 0.7 ceramics. *Sci. Rep.* **2021**, *11*, 17889.
(52) Yousefi, R.; Azimi, H. R.; Mahmoudian, M. R.; Basirun, W. J. The effect of defect emissions on enhancement photocatalytic performance of ZnSe QDs and ZnSe/rGO nanocomposites. *Appl. Surf. Sci.* **2018**, *435*, 886−893.
(53) Masalov, A. A.; Seminko, V. V.; Kononets, N. V.; Maksimchuk, P. O.; Bespalova, I. I.; Voloshina, L. I.; Malyukin, Yu.V. ZnSe nanocrystals obtained in pores of SiO2 matrix with temperature stable green luminescence. *J. Lumin.* **2017**, *181*, 337−344.
(54) Yousefi, R. Effects of Sn atoms on formation of ZnO nanorings. *CrystEngComm* **2015**, *17*, 2698−2704.
(55) Adolfová, L.; Dohnalová, Ž.; Šulcová, P. New inorganic pigments based on SrSnO 3 doped by V 2 O 5. *J. Therm. Anal. Calorim.* **2013**, *113*, 161−167.
(56) Yamashita, T.; Ueda, K. Blue photoluminescence in Ti-doped alkaline-earth stannates. *J. Solid State Chem.* **2007**, *180*, 1410−1413.
(57) Bohnemann, J.; Libanori, R.; Moreira, M. L.; Longo, E. High-efficient microwave synthesis and characterisation of SrSnO3. *Chem. Eng. J.* **2009**, *155*, 905−909.
(58) Singh, D. J.; Xu, Q.; Ong, K. P. Strain effects on the band gap and optical properties of perovskite SrSnO3 and BaSnO3. *Appl. Phys. Lett.* **2014**, *104*, 011910.
(59) Kumar, U.; Upadhyay, S. Structural, microstructure, optical, and dielectric properties of Sr1. 99M0. 01SnO4 (M: La, Nd, Eu) Ruddlesden−Popper oxide. *J. Mater. Sci.: Mater. Electron.* **2020**, *31*, 5721−5730.
(60) Singh, D. J.; Xu, Q.; Ong, K. P. Strain effects on the band gap and optical properties of perovskite SrSnO3 and BaSnO3. *Appl. Phys. Lett.* **2014**, *104*, 011910.
(61) Kumar, A. A.; Kumar, A.; Quamara, J. K.; Dillip, G. R.; Joo, S. W.; Kumar, J. Fe (III) induced structural, optical, and dielectric behavior of cetyl trimethyl ammonium bromide stabilized strontium stannate nanoparticles synthesized by a facile wet chemistry route. *RSC Adv.* **2015**, *5*, 17202−17209.
(62) Kumar, U.; Ankur, K.; Yadav, D.; Upadhyay, S. Synthesis and characterization of Ruddlesden-Popper system (Ba1− xSrx) 2SnO4. *Mater. Charact.* **2020**, *162*, 110198.
(63) Kumar, U.; Upadhyay, S. Studies on dielectric and electrical properties of Ruddlesden-Popper oxide Sr2SnO4. *Mater. Lett.* **2018**, *227*, 100−103.
(64) Neese, B.; Chu, B.; Lu, S. G.; Wang, Y.; Furman, E.; Zhang, Q. M. Large electrocaloric effect in ferroelectric polymers near room temperature. *Science* **2008**, *321*, 821−823.
(65) Ali, A.; Uddin, S.; Iqbal, Z.; Lal, M.; Jameel, M. H.; Zaman, A.; Ahmad, A.; Khan, W.; Khan, W. Synthesis and characterizations of (Ba1-xCax) Ti4O9, 0≤ x≤ 0.9 ceramics. *J. Mater. Res. Technol.* **2021**, *11*, 1828−1833.
(66) Baker, A.; Lanagan, M. T.; Semouchkina, E.; Semouchkin, G.; Kerr, T. Miniaturization of LTCC devices by using mixed dielectric substrates. In *3rd International Conference on Ceram. Interconnect and Ceramic Microsystems Technologies*; CICMT, 2007, pp 134−137.

https://doi.org/10.1021/acsomega.3c04224
ACS Omega 2023, 8, 33794−33801